Materials & Design 227 (2023) 111699

Contents lists available at ScienceDirect

Materials & Design

journal homepage: www.elsevier.com/locate/matdes

Machine learning for additive manufacturing: Predicting materials characteristics and their uncertainty

Dmitry Chernyavsky [a], Denys Y. Kononenko [a], Jun Hee Han [b], Hwi Jun Kim [b], Jeroen van den Brink [a], Konrad Kosiba [a]

[a] Leibniz Institute of Solid State and Materials Science (IFW Dresden), Helmholtzstr. 20, 01069 Dresden, Germany
[b] Korea Institute of Industrial Technology (KITECH), Korea Institute for Rare Metals, 156, Gaetbeol-ro, Yeonsu-gu, 21999 Incheon, South Korea

HIGHLIGHTS

- Additive manufacturing requires process control for the parts fabrication.
- A machine learning approach is proposed for processing parameters optimization.
- The approach provides tools for in-depth uncertainty quantification..
- The method is demonstrated by modeling the amorphicity of a glass-forming alloy.

GRAPHICAL ABSTRACT

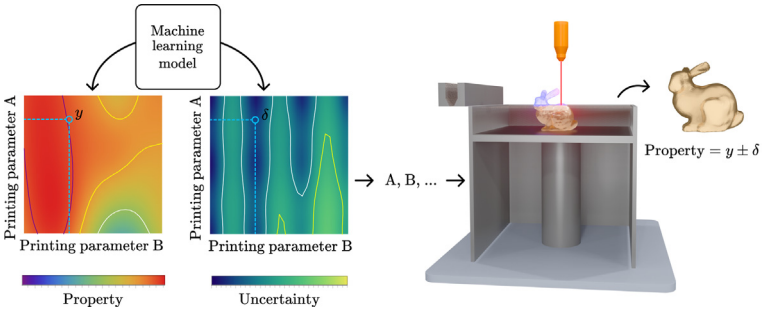

ARTICLE INFO

Article history:
Received 27 November 2022
Revised 3 February 2023
Accepted 4 February 2023
Available online 18 February 2023

Keywords:
Additive manufacturing
Laser powder bed fusion
Machine learning
Gaussian processes
Metallic glass
Uncertainty quantification

ABSTRACT

Additive manufacturing (AM) is known for versatile fabrication of complex parts, while also allowing the synthesis of materials with desired microstructures and resulting properties. These benefits come at a cost: process control to manufacture parts within given specifications is very challenging due to the relevance of a large number of processing parameters. Efficient predictive machine learning (ML) models trained on small datasets, can minimize this cost. They also allow to assess the quality of the dataset inclusive of uncertainty. This is important in order for additively manufactured parts to meet property specifications not only on average, but also within a given variance or uncertainty. Here, we demonstrate this strategy by developing a heteroscedastic Gaussian process (HGP) model, from a dataset based on laser powder bed fusion of a glass-forming alloy at varying processing parameters. Using amorphicity as the microstructural descriptor, we train the model on our $Zr_{52.5}Cu_{17.9}Ni_{14.6}Al_{10}Ti_5$ (at.%) alloy dataset. The HGP model not only accurately predicts the mean value of amorphicity, but also provides the respective uncertainty. The quantification of the aleatoric and epistemic uncertainty contributions allows to assess intrinsic inaccuracies of the dataset, as well as identify underlying physical phenomena. This HGP model approach enables to systematically improve ML-driven AM processes.

1. Introduction

Additive manufacturing (AM) - also known as three-dimensional (3D) printing - enables the fabrication of near-net shape components with high geometrical freedom, due to the layer-by-layer build-up based on a digital model [1–3]. Laser powder bed fusion (LPBF) is a widely used powder-bed based AM technology for the fabrication of metallic components [2]. A computer-controlled laser beam locally melts predestined volumes of a deposited thin powder layer (Fig. 1a). The molten volume fuses

https://doi.org/10.1016/j.matdes.2023.111699
0264-1275/

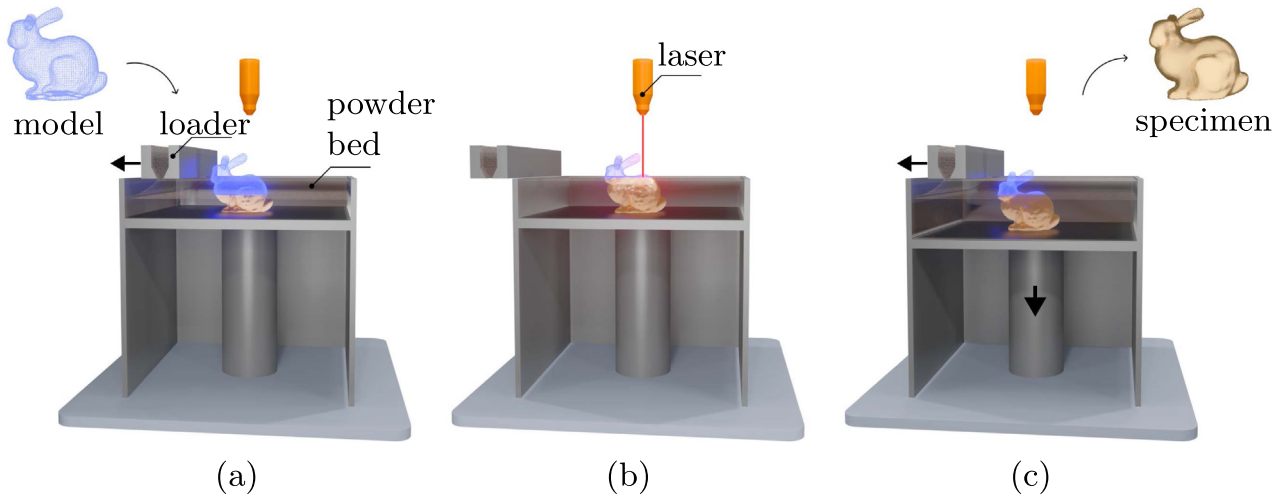

Fig. 1. Working principle of LPBF. During LPBF, a powder layer is deposited (a), and a focused laser-beam locally melts a specific volume according to a predetermined geometry. (b) The melt rapidly solidifies generating the first layer and, (c), the next powder layer is deposited and melted. This cycle is additively repeated, until the part is fully fabricated.

with the underlying material, so that one component's layer is completed (Fig. 1b). Afterwards, the next powder layer is deposited and melted (Fig. 1c). This cycle is repeated, until the build-up is completed [4]. (see Table 1).

Metal AM found its way into industry and still continues to be a transformative manufacturing process across multiple industrial sectors, such as aerospace, healthcare, energy and automotive [2,5]. Key challenges still remain with controlling the metal AM process rating high amongst them. Next to expensive printing equipment and feedstock material, a plethora of processing parameters must be correctly selected for the successful fabrication of components with desired microstructure ultimately determining their physical, functional and/ or mechanical properties [3,4]. Current practice to identify this so-called optimum processing parameter set is still based on trial and error [3], although the expertise of the AM-device operator as well as design of experiments [6] and statistical analyses [7,8] contribute to reduce the number of attempts required. All of these approaches are time-consuming and expensive which is especially valid for metal AM [2,9,10]. Since AM operates at the crossroad of materials, machines, computing and data [7], this innovative manufacturing technology is designed to be streamlined by automation [9,11,12]. Therefore, the application of data-driven ML methods would represent an alternative approach for the identification of the optimum parameter set. ML already found its way into metal AM, especially into LPBF [9–22].

One of the main focuses of ML applications to AM processing is the optimization of processing parameters based on property predictions of printed parts. The fundamental limitation of such a ML-based approach is the variability of the AM processes which is not adequately treated and captured by constructed ML models [23,24], so far. Physical processes, which govern the LPBF fabrication of parts, such as the interaction of the laser beam with metallic powder leading to its melting and subsequent solidification of the material are stochastic. Thus, a probability distribution to obtain a specimen with certain properties results at a given processing parameter set. To be more precise, variations can encompass powder characteristics (size and morphology of particles) and fluctuations of the laser power or scanning speed as well as further processing parameters. Next to the fabrication, also the characterization of specimens contributes to the resulting dispersion in the measured target properties [23,25]. Finally, ML models developed for predicting properties of additively manufactured materials also have a level of uncertainty depending on, for instance, the ML algorithms used to construct the models. All these various factors contribute to the resulting uncertainty that has to be properly treated.

The goal of the present work is twofold. Firstly, we intend to introduce ML methods for uncertainty quantification not previously used in the context of AM. The access to position-resolved uncertainty in the feature space is essential for designing smallest possible, but most efficient datasets for developing ML models with high predictive accuracy. As AM operator, one strives to produce and especially characterize as less as possible specimens required for generating the dataset used to develop the model. Therefore, it is of high interest to identify regions in the feature space with highest uncertainty, so that particularly the corresponding experimental datapoints are provided to the ML model for training. Furthermore, uncertainty quantification can be used to analyze the dataset for revealing underlying physical phenomena or measurement inaccuracy of LPBF-fabricated specimens. With the present work, we aim to demonstrate both, the identification of locations in the feature space with high uncertainty and the analysis of the experimental data used to develop the present ML model. Therefore, we generated a dataset based on laser powder bed fusion of a glass-forming $Zr_{52.5}Cu_{17.9}Ni_{14.6}Al_{10}Ti_5$ (at.%) alloy at varying processing parameters. This specific alloy was selected, because (partially) amorphous specimens can be fabricated by LPBF allowing to use the so-called amorphicity, which is a microstructural descriptor, as output label for the present ML model. The amorphicity is defined as the volume fraction of the amorphous phase of each (partially) glassy LPBF-fabricated specimen. In comparison to other microstructural descriptors, such as grain size and shape for crystalline materials, the amorphicity can be relatively easy accessed via differential scanning calorime-

Table 1
All the *RMSE* values are given in the units of the amorphous volume fraction (i.e., in %). $RMSE_{bulk}$ corresponds to the validation scheme in which, as the training data, all the boundary points were taken and the model was tested on the bulk points. $RMSE_{LOO}$ corresponds to the LOO cross-validation scheme. $RMSE_{LOO}$ (except one point) stands for the *RMSE* value corresponding to the LOO scheme performed for the dataset where the data point showing the greatest dispersion was removed.

$RMSE_{bulk}$	$RMSE_{LOO}$	$RMSE_{LOO}$(except one point)
1.12	2.58	1.69

try. By contrast the determination of grain size and shape require extensive and very time-consuming investigations involving metallurgical preparation and microscopic analysis. In consideration of a large number of specimens, which needed to be analyzed for generating a sufficient large dataset, selecting the amorphicty as output label is the logical choice. A salient feature of the experimental dataset is that its noise (uncertainty) level demonstrates heteroscedastic behavior. More precisely, the noise level inherent to the experimental data varies across the LPBF process parameter space for the specimens' fabrication. In order to construct a model with high predictive accuracy, one must adequately consider the heteroscedastic nature of the uncertainty inherent to the data. We thus use the HGP algorithm introduced in [26] to model interrelations between amorphicity and the LPBF processing parameters and determine the corresponding uncertainty level. Although Zr-based alloys have been extensively studied in recent years in the context of additively manufactured bulk metallic glasses [27–31], a robust model for accurate prediction of amorphicity dependent on the LPBF processing parameters has not been yet constructed. The development of such a model and its detailed analysis is hence our second main goal. The deliberate modulation of microstructural descriptors permits to design the microstructure and hence tailor the mechanical properties of LPBF-fabricated parts [32]. The present efforts are a first step toward exploiting the process-structure–property-performance linkage for the ML-driven fabrication of materials by additive manufacturing [11].

2. Experimental dataset

We aim to model the amorphicity and the corresponding uncertainty dependent on the LPBF processing parameters. From this perspective, it is important to have self-consistent data, which implies the employment of the machine with the same configuration for the production of the entire data, while the target characteristics should be measured using the same methods. Thus, we do not gather data for the Zr-based alloys from different sources but use a self-consistent experimental dataset from [33]. Laser power, scanning velocity and hatching distance were used as input parameters, because these processing parameters have been reported to mostly affect the amorphicity of specimens fabricated by LPBF from Zr-based glass-forming powder [28,34–36]. Of course, further processing parameters, such as thickness of the deposited powder layer or scanning strategy might also have an influence on the amorphicity. In order to demonstrate that a ML model can be successfully developed, those three most influential parameters were selected to predict the average amorphicity and respective uncertainty. Cuboid-like specimens ($5 \times 5 \times 10$ mm^3) were fabricated by processing powder with nominal composition of $Zr_{52.5}$ $Cu_{17.9}$ $Ni_{14.6}$ Al_{10} Ti_5 via LPBF using a SLM50 device (Realizer GmbH, laser spot size of 50 μm). A scanning strategy of unidirectional vectors rotated by 90°in neighboring layers was utilized and the powder layer thickness (40 μm) was held constant. For generating the dataset, the level of the three processing parameters were varied in such a manner that specimens with cuboid like shape were fabricated. Thereby, the fraction of defects like minor cracks and pores varied and depended on the exact processing parameters. The goal is to provide specimens with varying amorphicity, since the ML model also requires data from samples with low amorphicity to properly learn the interrelation between amorphicity and the three processing parameters. The selection of the exact levels is based on a previous study [28] and is for the three processing parameters as follows: laser power (90, 100, 110, and 120 W), scanning velocity (0.7, 0.8, 0.9, 1.0, and 1.1 m/s), and hatching distance (overlapping between adjacent melt tracks: 0.18, 0.2, and 0.22 mm). Three specimens were fabricated for each parameter set at the top, center and bottom location of the build plate to ensure reproducibility of the results leading to a total number of 180 specimens fabricated at six build jobs (Fig. 2). The measured amorphicity of the samples did not depend on the their print location and we intended only print iterations permitting the ML model to determine the uncertainty. Differential scanning calorimetry was conducted for all 180 samples (sample weight of about 25 mg) at a heating rate of 40 K/min using Al-crucibles in a Perkin-Elmer Diamond. Each sample was heated twice to 873 K to obtain a baseline required for determining the crystallization enthalpy. The amorphous volume fraction, which is defined as amorphicity, was determined from the measured crystallization enthalpy of each LPBF-fabricated specimen and subsequently normalized to the crystallization enthalpy of a fully amorphous specimen of same nominal composition which was prepared by copper-mold casting (Edmund Bühler GmbH). The dataset thus consists of 180 samples fabricated at 60 unique processing parameter sets.

3. Predicting model construction

Let us now turn to the ML model construction. In the ML community, one usually refers to the model's input data as *features*, while the output is called *target*. In our case, the LPBF processing parameters are features, and the amorphous volume fraction is the target. The task here is to predict the amorphicity based on a set of LPBF parameters. This is a classical regression problem to be tackled by applying a supervised ML algorithm. There are plenty of supervised ML algorithms in literature and the most profound ones among them, such as artificial neural networks, usually require a large training dataset. When dealing with medium-size structured data, decision tree-based algorithms (e.g., XGBoost [37] or Random Forests [38]), generally demonstrate the best predictive performance. The nature of tree-based algorithms leads to a non-smooth behavior of the produced response surfaces. The regression problem at hand, however, suggests that the response surface for the amorphous volume fraction should be described by a smooth function. Given the output variation to be fully determined by the three features at hand, while all other physical parameters that may influence the amorphicity of the specimens are constant, it is reasonable to expect that all points in the feature space within a close vicinity are correlated. The most suitable algorithm for such a task is the Gaussian process (GP) regression method [39]. Moreover, one main advantage of GP-based algorithms is that they also provide a natural framework for uncertainty quantification.

Based on given processing parameter values, proper application of GP-based algorithms allows to model the probability distribution for a certain property (e.g. amorphicity) of a specimen. However, the classical GP regression algorithm is only suited to

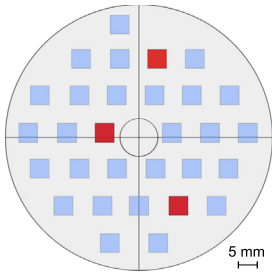

Fig. 2. Schematic illustration depicting the sample arrangement on the building plate. Ten times three samples with identical processing parameter set were fabricated at each building job. The red rectangles visualize three samples fabricated at identical parameter set and they were located in the top, center and bottom section of the build plate.

model the homoscedastic noise distribution, i.e. the noise which is constant for varying points of the feature space. As for each set of the LPBF parameters three specimens were produced and their amorphicity was measured, we may estimate the noise level inherent to these data. The scatter plot in Fig. 3 demonstrates that the lower amorphicity a specimen shows, the higher dispersion in its values was measured. One may also observe that the same trait is inherent to the feature space. The measured dispersion hence demonstrates heteroscedastic behavior, since it depends on the input data which shows varying levels of uncertainty for different regions of the feature space. As a consequence, classical GP regression algorithms requiring a homoscedastic noise distribution are not suited for modelling the interrelations between amorphicity and the processing parameters of the present dataset. Among GP regression methods, there is a family of algorithms known as heteroscedastic GP (HGP) [26,40,41] and they are more suited for the present dataset. These ML algorithms are designed to properly consider the heteroscedasticity in the noise level and are thus exploited to solve the present regression problem. Therefore, we exploited the HGP algorithm proposed in [26]. It should be noted that the classical (homoscedastic) GP algorithm has been previously applied by several authors to metal AM [20,10,42–49], including optimization of the LBPF processing parameters [20,10,49]. The HGP algorithm is, however, introduced to metal AM by the present study for the first time.

3.1. HGP regression algorithm

There are three features for the problem at hand: laser scanning velocity, hatching distance, and laser power. The input vectors $\mathbf{x}_i$ from the training dataset are aggregated in the matrix $X = (\mathbf{x}_1, \ldots, \mathbf{x}_n)^T$, while the corresponding target values are collected in the vector $\mathbf{y}$ with components y_i. In the present case, each vector $\mathbf{x}_i$ consists of three components, corresponding to the three LPBF processing parameters. We assume a Gaussian noise term contribution for the measured training data which depends on the input data. To be more precise, it is assumed that the measured amorphicity data, y_i, is approximated by $y_i = f(\mathbf{x}_i) + \epsilon_i$, where f is a Gaussian process prior and $\epsilon_i \sim \mathcal{N}(0, \sigma_i)$ is a Gaussian noise term. The dispersion parameters σ_i for ϵ_i are defined by a function $\sigma_i^2 = r(\mathbf{x}_i) = \mathbf{r}$, which is to be identified during the fitting procedure. Denoting a point in the feature space which shall be predicted by $\mathbf{x}_*$, the HGP regression algorithm gives mean m_* and standard deviation σ_* values for the corresponding target according to following relations:

$$\begin{aligned} m_* &= K(\mathbf{x}_*, X)[K(X,X) + R(X)]^{-1}\mathbf{y}, \\ \sigma_*^2 &= \sigma_a^2 + \sigma_e^2, \end{aligned} \tag{1}$$

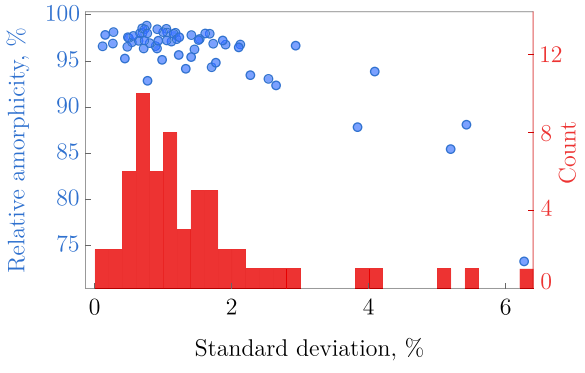

Fig. 3. (Color online) Distribution of the standard deviation of the experimentally measured data points.

where

$$\begin{aligned} \sigma_a^2 &= R(\mathbf{x}_*), \\ \sigma_e^2 &= K(\mathbf{x}_*, \mathbf{x}_*) \\ &\quad -K(\mathbf{x}_*, X)[K(X,X) + R(X)]^{-1}K(X, \mathbf{x}_*), \end{aligned} \tag{2}$$

and R is the diagonal matrix $R(X) = \mathrm{diag}(\mathbf{r})$, while $R(\mathbf{x}_*) = r(\mathbf{x}_*)$. The central object of any GP algorithm is the kernel $k(\cdot,\cdot)$, defining the expressions above as

$$K(X,X) = \begin{bmatrix} k(\mathbf{x}_1,\mathbf{x}_1) & \ldots & k(\mathbf{x}_1,\mathbf{x}_n) \\ \vdots & \ddots & \vdots \\ k(\mathbf{x}_n,\mathbf{x}_1) & \ldots & k(\mathbf{x}_n,\mathbf{x}_n) \end{bmatrix}, \tag{3}$$

together with

$$\begin{aligned} K(\mathbf{x}_*, X) &= (k(\mathbf{x}_*,\mathbf{x}_1), \ldots, k(\mathbf{x}_*,\mathbf{x}_n)), \\ K(X, \mathbf{x}_*) &= K^T(\mathbf{x}_*, X), \end{aligned} \tag{4}$$

and $K(\mathbf{x}_*, \mathbf{x}_*) = k(\mathbf{x}_*, \mathbf{x}_*)$. The ability to predict the standard deviation is the basis for the uncertainty quantification analysis demonstrated in this work. The meaning of variances σ_a^2 and σ_e^2 will be explained in the following sections.

The HGP and classical (homoscedastic) GP regression algorithms mainly differ in the term $R(\cdot)$, which in the case of classical GP has to be replaced by the identity matrix $\mathbb{I}$ multiplied by a constant parameter σ_n^2 [39]. The kernel function $k(\cdot,\cdot)$ determines the generalization properties of the HGP model. For example, if one deals with data demonstrating periodic behavior, the best choice for the model construction would be to take a periodic kernel. However, the proper selection of the structural form of the kernel for most ML problems is somehow a black art [50]. In general, a common strategy is to use a kernel function from the Matérn class of kernels. In order to construct the present HGP model, we chose the Matérn-3/2 function which is defined by

$$k(\mathbf{x}_i, \mathbf{x}_j) = A^2\left(1 + \sqrt{3}d(\mathbf{x}_i, \mathbf{x}_j)\right)e^{-\sqrt{3}d(\mathbf{x}_i,\mathbf{x}_j)}.$$

One may think of $d(\mathbf{x}_i, \mathbf{x}_j)$ as a metric in the feature space and it (its squared value) can be written as

$$d^2(\mathbf{x}_i, \mathbf{x}_j) = (\mathbf{x}_i - \mathbf{x}_j)^T M(\mathbf{x}_i - \mathbf{x}_j), \tag{6}$$

where M is the diagonal matrix $M = \mathrm{diag}(\mathbf{l})^{-2}$. In our case, there are three non-vanishing components $\mathbf{l} = (l_P, l_v, l_h)$ of the matrix which correspond to laser power, laser velocity and hatching distance, respectively. These parameters strongly affect the characteristic length scales which, in a sense, define how far one needs to move along one particular axis in the feature space to observe a significant change in the target values. The parameter A^2 is usually called signal variance and defines the kernel function amplitude. The constant parameters described above are usually called *hyperparameters*, and in what follows, we will refer to them by the symbol θ. Thus, in our case $\theta = (\mathbf{l}, A)$. The hyperparameters must be identified during the fitting procedure of the present HGP regression model.

3.1.1. Fitting procedure

The main idea behind the algorithm proposed in [26] is to estimate the uncertainty level from the training data and to build an additional model to accurately predict it. To do so, one can perform the following steps. Firstly, a classical (homoscedastic) GP model, G_1, is fitted using the training data. By definition, this model predicts a multivariate probability distribution for the target. In the next step, for each training input $\mathbf{x}_i$, one takes a number s of target values $y_i^{(p)}$ from the distribution generated by the model G_1 and estimates the noise level according to following formula:

$$r(\mathbf{x}_i) = \frac{1}{2s}\sum_{p=1}^{s}\left(y_i - y_i^{(p)}\right)^2, \tag{7}$$

where y_i is the predicted mean value of the target at point $\mathbf{x}_i$. In our model, we use the number of samples as $s = 100$. This step is followed by training another GP model, G_2, for which target is the noise level $R(X)$. Mean values predicted by G_2 for the training input define the term $R(X)$ which is used to fit the model G_1 at the following step. Thus, G_1 is fitted with the noise term $R(X)$ predicted by G_2, in all the subsequent iterations. The cycle should be repeated until it converges. In our experiments, about ten iterations were, therefore, needed.

All hyperparameters are optimized following the marginal likelihood maximization procedure [39]. The log marginal likelihood is defined by

$$\begin{aligned}\mathscr{L}(\theta) = &-\tfrac{1}{2}\mathbf{y}^T(K(X,X)+R(X))^{-1}\mathbf{y}\\ &-\tfrac{1}{2}\log\det\left(K(X,X)+R(X)\right)-\tfrac{n}{2}\log 2\pi,\end{aligned} \tag{8}$$

which is a function of hyperparameters θ that are optimized to maximize the function $\mathscr{L}$. In the first iteration of the fitting algorithm, for the G_1 model, the matrix R should be replaced by a diagonal matrix with the constant noise term $\sigma_n^2\mathbb{I}$ which also has to be fitted. At all following iterations, one fits the model by minimizing the likelihood function with the noise level R predicted by the model G_2.

4. ML modeling of the amorphous volume fraction

Following the algorithm described above, a HGP model was developed (the source code for the HGP algorithm is available in a GitHub repository [51]). The predicted mean and uncertainty (standard deviation) values for amorphicity are depicted in Figs. 4 and 5, respectively. In the following, we will discuss the model performance and describe the influence of the LPBF parameters on amorphicity.

4.1. Model's performance

The creation of a dataset by metal AM technologies is generally laborious and cost-intensive, due to the processing of the feedstock and especially characterization of the resulting specimens [19]. As a consequence, relatively small datasets of high quality are mostly provided for developing ML models, such as the present HGP model. For the development of a ML model, the dataset must be split for training and testing, so that "overfitting", which is a statistical challenge for ML in general [52], is avoided. Testing reveals whether the model really "learned" the underlying interrelations between the output (e.g. amorphicity) and the features (e.g. processing parameters) and hence "generalizes", or whether it is overfitted during training. In order to fully exploit the dataset for developing an accurate model, the so-called k-fold cross-validation (CV) [39] can be used. Within the k-fold CV approach, the dataset is randomly split into k groups of equal size known as folds. One of the folds is used for testing, whereas the residual folds are used for training. However, for the present small dataset, the experimental matrix design has a subtlety: Removing just a small number of points would lead to a large region of the feature space uncovered, leaving the model without knowledge of the target behavior in this particular region. Yet, it is reasonable to expect the model to have good interpolation abilities. Let us remind that the training points form a cubic lattice. There are 54 points on the boundary of this cube and six points lie in the bulk. Using boundary points as a training dataset, while the bulk ones as test data, one may find the root-mean-squared error (RMSE) to be 1.12%. Compared to the range of the original observed amorphicity values, the RMSE is reasonably low. k-fold CV can be carried out to the extreme by splitting the dataset into the number of data-vectors, so that each data-vector is used once for testing and all residual ones for training. This split method is known as leave-one-out cross-validation (LOO CV), which we exploit in order to get insight into the extrapolation properties of our model. Recalling that for each point of the feature space three samples were fabricated, we define a performance metric

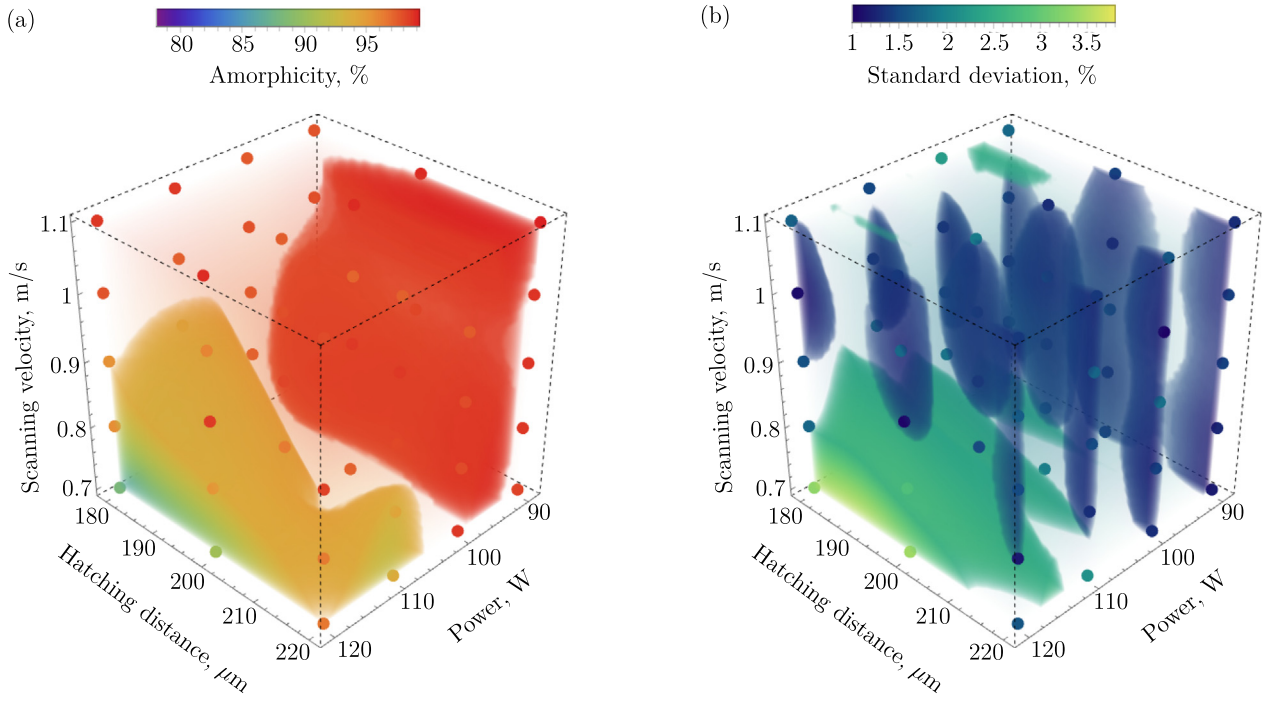

Fig. 4. (Color online) HGP model predictions for mean values of amorphicity (a) and its total uncertainty (b).

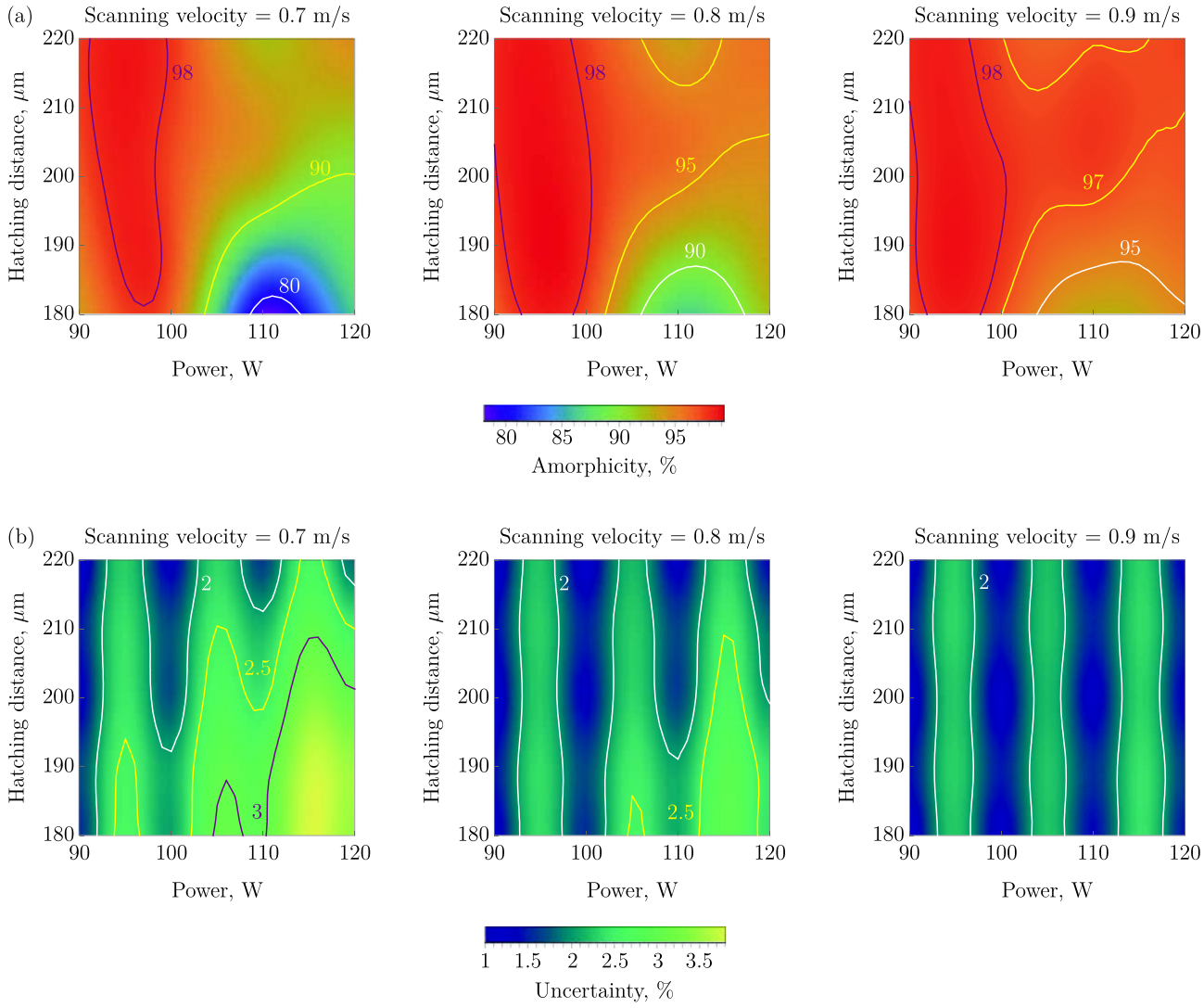

Fig. 5. (Color online) Two-dimensional contour maps of HGP model predictions for mean values of amorphicity (a) and its total uncertainty (b).

$$RMSE_{LOO} = \sqrt{\frac{1}{n}\sum_{i=1}^{n}\left(\langle y_i^{exp}\rangle - y_i^{pred}\right)^2},$$

where n is equal to the number of parameter sets used to generate the experimental dataset ($n = 60$). Here $\langle y_i^{exp}\rangle$ stands for an averaged value of amorphicity over three samples for a point in the feature space i, while y_i^{pred} is the corresponding mean value predicted by the HGP model according to Eq. (1). The present model yields an $RMSE_{LOO}$ of 2.58%. In other words, it predicts the amorphicity at a given processing parameter set with an accuracy of 2.58%. We note that this error is rating the overall predictive performance of our HGP model, but not the position-resolved uncertainty of an output-inputs vector of the feature space. Certain points of the dataset used for developing this model are crucial. When performing the LOO CV, the largest contribution to the resulting error stems from points with lowest amorphicity and their neighboring data points (these are the points in the left bottom corner in Fig. 4). The model is not able to adequately capture a drastic change in amorphicity in the vicinity of this region when the corresponding data points are removed from the training dataset. This fact is also reflected in the high experimentally measured dispersion which will be discussed below. If removing only one point with the highest experimentally measured dispersion prior to performing LOO CV, the $RMSE_{LOO}$ significantly drops down to 1.69%.

4.2. Amorphicity dependence on the LPBF processing parameters

The aim of the HGP model is to accurately predict the amorphicity for the three given processing parameters. Following the fitting procedure described in the previous section, this model was developed using the complete experimental dataset. Fig. 4a displays the mean values of the predicted amorphicity as a function of the three features (laser power, scanning velocity, hatching distance), thus covering the three-dimensional features space. Fig. 5a allows a more quantitative perception of the amorphicity by illustrating the corresponding mean values in two-dimensional contour maps of this space at varying scanning velocity. In general, the amorphicity of the specimens is higher when lower laser powers and larger values for the hatching distance and scanning velocity were employed during their LPBF-fabrication as is in line with literature [35,53,28,33]. In particular, the contour maps shown in Fig. 5a disclose two characteristic regions. At low laser powers up to about 100 W, the LPBF-fabricated specimens showed high mean values down to 98% for amorphicity. Interestingly, amorphicity is hardly affected by the scanning velocity and hatching distance in this

region. By contrast, both processing parameters have a strong impact on amorphicity when a laser power higher than 100 W was employed for LPBF fabrication. Then the amorphicity strongly varies with scanning velocity and also hatching distance. A drastic drop in amorphicity from 95 – 80% was observed with decreasing scanning velocity from 0.9 – 0.7 m/s (Fig. 5a). Since highly amorphous specimens are fabricated by LPBF in the first processing regime, higher cooling rates must be then effective. The volume fraction of the vitrified phase – its amorphicity – is determined by the exact cooling rate which the utilized processing parameters dictate. The heat from the consecutively molten pools is extracted through the underlying solid material [4]. The speed of heat extraction determines the cooling rate and depends on the thermophysical properties of the underlying solid and especially on the processing parameters. There is no access to alter the materials properties, but variation of the processing parameters allows to adjust the cooling rates. They must be sufficiently high to circumvent intervening crystallization and in turn favor vitrification. Low laser powers, fast scanning velocities and large hatching distances thus favor amorphicity or are more efficient in preventing crystallization during LPBF-processing.

5. Uncertainty modeling

Gaussian process-based models, such as the present HGP algorithm, provide a natural framework to quantify the uncertainty of the predicted mean values for an output label of choice (e.g. amorphicity). This means that the model provides a position-resolved uncertainty for any mean value in the feature space, unlike the RMSE value rating the performance accuracy of the GP model (see Section 4.1). The access to position-resolved uncertainty is almost invaluable for generating smallest possible datasets which still allow for developing ML models with high predictive accuracy. This advantage is decisive especially for optimizing metal AM processing, since the generation of a dataset, which is tantamount to the fabrication and characterization of specimens, is time- and cost-intensive. Therefore, one aims to provide an absolute minimum number of experimental points to the ML algorithm to construct the respective model. In order to efficiently enhance its predictive accuracy, data points in the feature space with highest uncertainty must be identified, so that the corresponding specimens can be fabricated and characterized. The current HGP model exactly enables the identification of data points with high uncertainty. It additionally allows to understand the higher uncertainty in the feature space by providing the uncertainty contributions. This approach is demonstrated in the following by the uncertainty distribution of the amorphicity as a function of the processing parameters. Fig. 4b displays a three-dimensional plot of the total uncertainty as a function of the three features: scanning velocity, hatching distance and laser power. Highest values of the standard deviation calculated according to Eq. (1), which is a measure for the total uncertainty predicted by the HGP model, are observed in a contiguous region above a laser power of 100 W, below a scanning velocity of 0.9 m/s, and at a decreasing hatching distance (Fig. 4b, bottom left corner). Lowest mean values for amorphicity exactly characterize this particular region of the feature space, as Fig. 4a proves. Possible reasons could stem from the intervening crystallization or the measurement accuracy of the amorphicity by DSC, and we are going to elaborate on these reasons later on. Higher values of the uncertainty can be, furthermore, found in regions located between the experimental data points. In other words, the total uncertainty shows lowest values in the vicinity of the training points, while distant points are characterized by higher uncertainty [39].

For the present HGP model, higher uncertainty can be found in regions periodically arranged in the feature space forming a layered structure of larger uncertainty. The respective two-dimensional contour plots (Fig. 5b) point out this layered structure. Larger uncertainty is clearly visible between the experimental data points in the contour plot at a constant scanning velocity of 0.9 m/s. The dispersion length differs along the three features. Otherwise, uncertainty would have been concentrated in regions with a cuboid-like shape in the feature space located between the experimental points which are defined by the three features. This is not the case, since contiguous layered regions of larger uncertainty are present at constant laser powers (Figs. 4b and 5b). A possible explanation for this uncertainty distribution pattern is the following. After having fitted the model, one may check that the length scale l_P in Eq. (5) for laser power has the lowest value compared to the other features. The correlation length defines how far one should move along the corresponding axis to see a significant change in the target values. The lower value the length scale has for a particular feature, the weaker correlation will the points along the axis defined by the feature have [39]. When varying the feature laser power and moving away from the experimental points along the laser power axis, a higher uncertainty results than by varying the other feature values.

5.1. Aleatoric and epistemic uncertainty

The total uncertainty is distributed in the feature space within two characteristic structures (Figs. 4b and 5b): (i) a contiguous region demarcated by low scanning velocities (below 0.9 m/s) and higher laser powers (above 100 W), and (ii) the layered structure. This finding could indicate two different sources of uncertainty. In machine learning often a distinction of uncertainty may appear unnecessary, because the ML model is asked to make a prediction for an output and the exact source of its uncertainty may be then irrelevant [54]. If, however, the aim is directed towards understanding the dataset for ultimately reducing the uncertainty of the ML model, a distinction of the corresponding sources is vital. Any source of uncertainty can be generally categorized as either *aleatoric* or *epistemic* [55,54]. Aleatoric uncertainty is inherent in the observations. To be more precise, the outcome of a specific experiment, such as e.g. "coin flipping" is dictated by inherently random effects [54]. Consequently, this type of uncertainty cannot be reduced by gathering more knowledge or improving the predicting model. By contrast, the epistemic uncertainty originates from a lack of knowledge and can be in principle reduced by providing additional information for training the model [54].

The predicted standard deviation values, σ_* , were calculated according to Eq. (1) and they are comprised of an aleatoric and epistemic uncertainty contribution (see, e.g., [56]). The aleatoric noise level is governed by the term σ_a from Eq. (2), while σ_e corresponds to the model's epistemic uncertainty. Figs. 6a and 6b display the aleatoric and epistemic distribution values predicted by the HGP model, respectively. The modeled aleatoric part properly captures the noise level behavior arising from the training dataset and comprises the contiguous region demarcated by low scanning velocities and higher laser powers, as also displayed in Fig. 4b. Thus, the aleatoric contribution poses one source of the total uncertainty. Fig. 6b visualizes the predicted epistemic uncertainty also obtained from the training set. Highest values for the standard distribution are located in regions between the experimental data points readily characterized by a layered structure. Since, the superposition of Figs. 6a and 6b yield the total uncertainty visualized in Fig. 4b, the epistemic part is hence the second source of the total uncertainty.

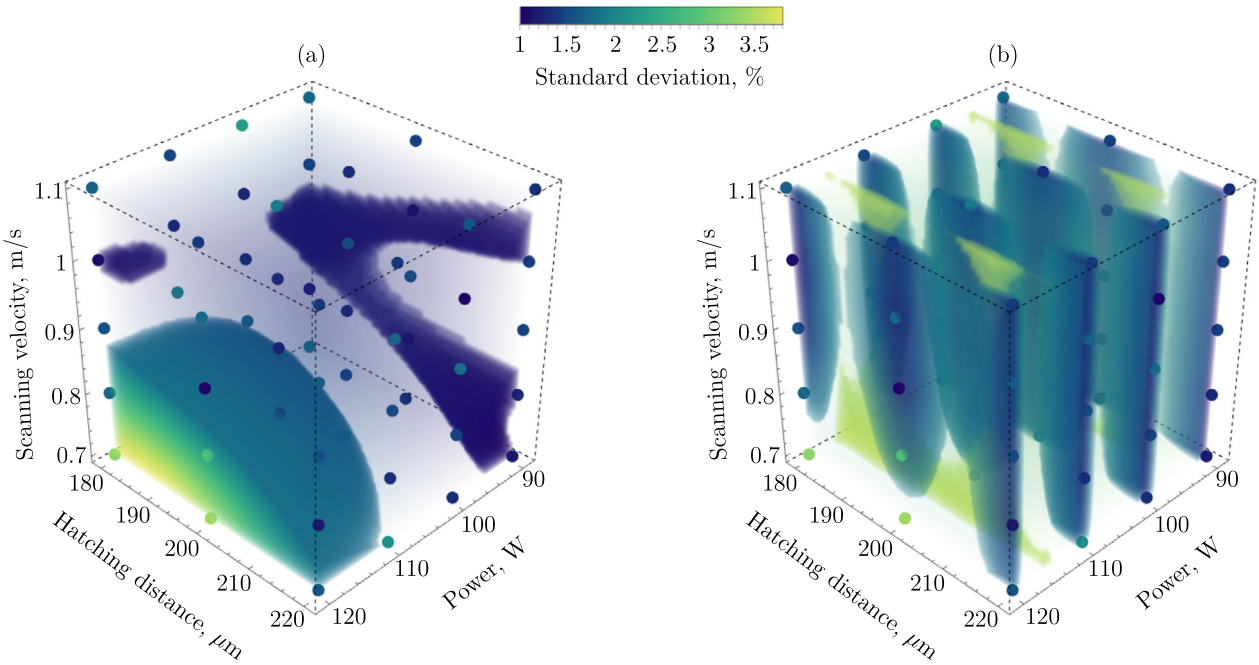

Fig. 6. (Color online) Position-resolved (a) aleatoric and (b) epistemic uncertainties predicted by the HGP model.

As previously mentioned, uncertainty quantification can be a powerful tool to design small datasets specifically for developing ML models with high predictive accuracy. The aim is to produce a minumum number of experimental datapoints required for model construction. The ability to separate the total uncertainty into the aleatoric and epistemic contributions is therefore the basis. The epistemic uncertainty is highest in the uncovered feature space (Fig. 6b) reaching a maximum in between the experimental data points. Therefore, this uncertainty contribution can be reduced by providing additional data points of uncovered feature space. By contrast, the aleatoric uncertainty contribution cannot be reduced by training the HGP model with additional experimental data points and instead strongly depends on the measured amorphicity, as depicted by Figs. 4a and 4b. In order to efficiently improve the model, further experimental data points shall be generated for regions with highest uncertainty. A strategy is to determine the maximum value of the epistemic uncertainty which yields a threshold value, as displayed in Fig. 7 (red dotted line) highlighting the dependence of the total uncertainty on the laser power at constant hatching distance and velocity. One must generate additional datapoints for locations with higher uncertainty than this threshold value. Then the epistemic part is eliminated, so that only the aleatoric contribution remains. The separation into epistemic and aleatoric uncertainty contributions hints at whether performing new measurements would improve the model's performance. Eliminating epistemic uncertainty, by definition, improves the predicting power of the model. If the aleatoric uncertainty gives the prevailing contribution to the total one in some region, adding new points in that region would not (significantly) improve the model performance. A way to circumvent this issue is to identify sources of the aleatoric uncertainty followed by revising the experimental procedure, especially the characterization method. This is the focus of the following section. Nevertheless, in order to testify the described strategy in full scale, the fabrication of additional samples for the identified processing parameters is required. This is the subject of future research activities and hence beyond the scope of the present work.

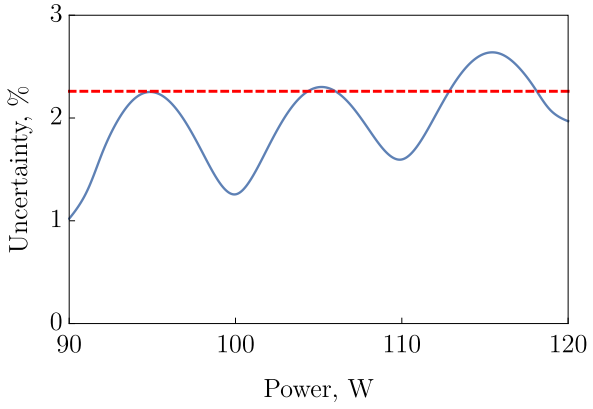

Fig. 7. Uncertainty distribution dependence on power at fixed values of laser velocity, 0.8 m/s, and hatching distance, 200 μm. The red dotted line corresponds to the acceptable uncertainty level.

5.2. Sources for uncertainty

During LPBF, crystallization can either occur during initial (partial) vitrification of the melt or is induced into the bulk metallic glass during subsequent cyclic re-heating, due to the layer-by-layer fabrication [35]. During the vitrification of the overlying layers, the heat is extracted through the underlying material which then experiences a heat treatment. Previously formed glass is reheated above the glass-transition temperature, so that it devitrifies into a supercooled liquid [57,58]. At further heating, supercritical nuclei will form and continue to grow leading to (partial) crystallization of the affected volume. The molten pools will be heated to higher temperatures, when increasing laser powers, decreasing scanning velocities and lower hatching distances are employed during LPBF. More heat must be then extracted resulting in lower cooling rates effective during solidification of the molten pools [59] and resulting in also stronger heating of the underlying material. In this process regime, crystallization of the supercooled liquid

is more likely to occur, in turn leading to lower amorphicity. The LPBF process yields reproducible results, since identical powder is processed at same conditions to fabricate multiple samples with same microstructure. The size, shape and maximum temperature of the molten pools are equal, since they are determined by the same processing parameters. As a consequence, all samples should show a similar amorphous volume fraction eventually with crystals uniformly distributed throughout the whole sample. Thus, LPBF fabrication of the samples most likely does not contribute significantly to the characteristic uncertainty observed in Fig. 6a (bottom left corner).

The next step for generating the experimental dataset used for training the HGP model was the measurement of the amorphous volume fraction using differential scanning calorimetry. The corresponding measurement can be only carried out with a certain resolution. Furthermore, a baseline was generated to extract the crystallization enthalpy used for calculating the amorphicity. The measurement and analysis thus involve an error characterized by a certain absolute value [60]. This absolute value has a stronger impact on samples with lower absolute values of the crystallization enthalpy ultimately leading to a less accurate determination of the amorphicity, as Fig. 3 proves. The aleatoric uncertainty is increasing with smaller values of amorphicity. Thus, this behavior originates from the input-dependent uncertainty so that the amorphous volume fraction has higher dispersion above a laser power of 100 W and below a scanning velocity of 0.9 m/s (Fig. 6a).

6. Conclusions

Here, we have introduced a HGP model for accurate modeling of materials properties and uncertainty quantification. The realization of such a ML-driven approach for the fabrication of materials with predestined microstructure and resulting properties, was successfully demonstrated by modeling the amorphous volume fraction – the amorphicity – of $Zr_{52.5}$ $Cu_{17.9}$ $Ni_{14.6}$ Al_{10} Ti_5 specimens fabricated by LPBF. The amorphicity served as exemplary property. Altogether, the used dataset consists of 180 Zr-based fabricated samples at 60 unique combinations of varied laser power, scanning velocity and hatching distance. The amorphicity was determined via differential scanning calorimetry for all fabricated specimens. The developed HGP model shows an accurate predictive performance characterized by a root mean square error (RMSE) of 1.12%. Based on the predicted amorphicity, two characteristic regions of the feature space can be distinguished: A highly amorphous region was observed when laser powers below 100 W were used for the LPBF fabrication of the Zr-based specimens. The amorphicity of this region is hardly affected by varying scanning velocities and hatching distances. By contrast, the second region characterized by laser powers above 100 W shows a strong influence of the residual processing parameters. The amorphicity drops down to below 80% when additionally, low hatching distances and slow scanning velocities were used for LPBF fabrication.

The HGP model was designed to not only predict the mean values of the amorphicity position-resolved in the feature space, but also to quantify the aleatoric and epistemic uncertainty contributions. The total uncertainty is distributed in the feature space within two characteristic structures which correspond to each uncertainty contribution. The epistemic uncertainty characterized by high values of the standard deviation is located in regions between the experimental data points forming a layer-like structure. This uncertainty source can be reduced by providing additional data points of uncovered feature space. By contrast, more training data points would not reduce the aleatoric uncertainty contribution, which in the present case strongly depends on the measured amorphicity. The aleatoric uncertainty is inherent to the training dataset and showed highest values of the standard deviation within a contiguous region demarcated by low scanning velocities and higher laser powers. This uncertainty contribution originated from the limited measuring accuracy of the differential scanning calorimetry device used for determining the amorphicity. Lower values of amorphicity were measured less accurate. Thus, the present HGP model does not only predict the amorphicity of Zr-based specimens fabricated by LPBF at a given processing parameter set with high accuracy, but it additionally provides the uncertainty of the respective mean value. Furthermore, this model serves as analysis tool for the investigation of the dataset used for training. Limited measurement accuracy or the random influence of underlying physical phenomena can be revealed by the aleatoric uncertainty contribution. The conceptualization of the dataset with respect to selected levels and their number of the processing parameter combinations determine the epistemic uncertainty. Insights into the uncertainty of the predicted mean values for a certain microstructural descriptor (e.g. amorphicity) or property are vital for an AM device operator who uses an HGP model as a guiding map for the selection of optimum LPBF processing parameters. This additional information allows him to evaluate the quality of the dataset and to possibly reveal processing parameter combinations with high uncertainty of the property. By generating additional experimental datapoints, the corresponding epistemic contribution is eliminated, so that the total uncertainty in this region is reduced. This resource-efficient strategy yields a HGP model with even higher predictive accuracy. The constructed HGP model has, however, limitations. Its extrapolation properties are not reliable for uncovered regions of the feature space spanned by the LPBF processing parameters. This is particularly valid for uncovered regions far away from the experimental data points used for constructing the HGP model and the predicted epistemic uncertainty demonstrates this fact. We note that this limitation does not depend on the ML algorithm on its own and can be only overcome by providing additional experimental data points.

Along this line we would like to address possible further developments of the present work. The GP family of algorithms is widely known in the Bayesian optimization context. Thus, the next logical step would be the combination of the presented HGP approach with Bayesian optimization methods. The presence of heteroscedastic noise, however, poses a challenge for Bayesian optimization and ongoing research activities within the ML community are focusing on this problem (see, e.g, [56]). We believe that the incorporation of Bayesian optimization tools into the presented HGP method may result in the development of a more effective approach for the optimization of LPBF processing and this is the focus of upcoming works.

7. Data availability statement

Data is available from the corresponding author on reasonable request.

Data availability

Data will be made available on request.

Declaration of Competing Interest

The authors declare that they have no known competing financial interests or personal relationships that could have appeared to influence the work reported in this paper.

Acknowledgments

We thank N. Geißler and P.G.K. Seethapettai for experimental support and Sergio Scudino for stimulating discussions. The work of D.C. was supported by the Alexander von Humboldt Foundation. K.K. acknowledges the financial support from the German Research Foundation (DFG KO 5771/1–1) and the Leibniz Association.

References

[1] T. Mukherjee, T. DebRoy, Appl. Mater. Today 14 (2019) 59.
[2] T. DebRoy, T. Mukherjee, J. Milewski, J. Elmer, B. Ribic, J. Blecher, W. Zhang, Nat. Mater. 18 (2019) 1026.
[3] T. DebRoy, H. Wei, J. Zuback, T. Mukherjee, J. Elmer, J. Milewski, A.M. Beese, A. d. Wilson-Heid, A. De, and W. Zhang, Progress in Materials Science 92, 112 (2018).
[4] W.E. King, A.T. Anderson, R.M. Ferencz, N.E. Hodge, C. Kamath, S.A. Khairallah, A.M. Rubenchik, Appl. Phys. Rev. 2 (2015) 041304.
[5] T.M. Pollock, Nat. Mater. 15 (2016) 809.
[6] B. AlMangour, Additive manufacturing of emerging materials, Springer, 2019.
[7] J. Sun, Y. Yang, D. Wang, Opt. Laser Technol. 49 (2013) 118.
[8] A. Pawlak, M. Rosienkiewicz, E. Chlebus, Arch. Civil Mech. Eng. 17 (2017) 9.
[9] X. Qi, G. Chen, Y. Li, X. Cheng, C. Li, Engineering 5 (2019) 721.
[10] G. Tapia, S. Khairallah, M. Matthews, W.E. King, A. Elwany, Int. J. Adv. Manuf. Technol. 94 (2018) 3591.
[11] C. Wang, X. Tan, S. Tor, C. Lim, Addit. Manuf. 36 (2020) 101538.
[12] L. Meng, B. McWilliams, W. Jarosinski, H.-Y. Park, Y.-G. Jung, J. Lee, J. Zhang, Jom 72 (2020) 2363.
[13] C. Kamath, The International Journal of Advanced Manufacturing Technology 86 (2016) 1659.
[14] H.S. Park, D.S. Nguyen, T. Le-Hong, X. Van Tran, J. Intell. Manuf. 1 (2021).
[15] L. Scime, J. Beuth, Additive Manufacturing 24 (2018) 273.
[16] L. Scime, J. Beuth, Additive Manufacturing 25 (2019) 151.
[17] X. Shen, J. Yao, Y. Wang, J. Yang, in: International Symposium on Neural Networks, Springer, 2004, pp. 832–840.
[18] S.A. Shevchik, C. Kenel, C. Leinenbach, K. Wasmer, Additive Manufacturing 21 (2018) 598.
[19] C.H. Lee, U. Kühn, S.C. Lee, S.J. Park, H. Schwab, S. Scudino, K. Kosiba, et al., J. Alloy. Compd. 862 (2021) 158018.
[20] G. Tapia, A.H. Elwany, H. Sang, Additive Manufacturing 12 (2016) 282.
[21] S. Liu, A.P. Stebner, B.B. Kappes, X. Zhang, Additive Manufacturing 39 (2021) 101877.
[22] Q. Liu, H. Wu, M.J. Paul, P. He, Z. Peng, B. Gludovatz, J.J. Kruzic, C.H. Wang, X. Li, Acta Mater. 201 (2020) 316.
[23] Z. Hu, S. Mahadevan, Scripta materialia 135 (2017) 135.
[24] Z. Wang, P. Liu, Y. Ji, S. Mahadevan, M.F. Horstemeyer, Z. Hu, L. Chen, L.-Q. Chen, Jom 71 (2019) 2625.
[25] F. Lopez, P. Witherell, B. Lane, J. Mech. Des. 138 (2016).
[26] K. Kersting, C. Plagemann, P. Pfaff, and W. Burgard, in Proceedings of the 24th international conference on Machine learning (2007) pp. 393–400.
[27] M. Mohr, R.K. Wunderlich, D.C. Hofmann, and H.-J. Fecht, npj Microgravity 5, 1 (2019).
[28] S. Pauly, C. Schricker, S. Scudino, L. Deng, U. Kühn, Materials & Design 135 (2017) 133.
[29] N. Sohrabi, J.E. Schawe, J. Jhabvala, J.F. Löffler, R.E. Logé, Scripta Mater. 199 (2021) 113861.
[30] Y. Li, Y. Shen, C.-H. Hung, M.C. Leu, H.-L. Tsai, Materials Science and Engineering: A 729 (2018) 185.
[31] Y. Li, Y. Shen, M.C. Leu, H.-L. Tsai, Materials Science and Engineering: A 743 (2019) 404.
[32] P. He, Q. Liu, J.J. Kruzic, X. Li, Mater. Lett. 307 (2022) 131018.
[33] K. Kosiba, D.Y. Kononenko, D. Chernyavsky, L. Deng, J. Bednarcik, J. Han, J. van den Brink, H.J. Kim, S. Scudino, J. Alloy. Compd. (2023) 168946.
[34] L. Deng, L. Zhang, K. Kosiba, R. Limbach, L. Wondraczek, G. Wang, D. Gu, U. Kuehn, S. Pauly, Journal of Materials Science & Technology 81 (2021) 139.
[35] D. Ouyang, P. Zhang, C. Zhang, L. Liu, Applied Materials Today 23 (2021) 100988.
[36] L. Deng, A. Gebert, L. Zhang, H. Chen, D. Gu, U. Kühn, M. Zimmermann, K. Kosiba, S. Pauly, Materials & Design 189 (2020) 108532.
[37] T. Chen and C. Guestrin, in Proceedings of the 22nd ACM SIGKDD International Conference on Knowledge Discovery and Data Mining, KDD '16 (ACM, New York, NY, USA, 2016) pp. 785–794.
[38] T.K. Ho, in Proceedings of 3rd international conference on document analysis and recognition, Vol. 1 (IEEE, 1995) pp. 278–282.
[39] C.E. Rasmussen, C.K.I. Williams, Gaussian processes for machine learning., Adaptive computation and machine learning, MIT Press, 2006. pp. I-XVIII, 1–248..
[40] Q.V. Le, A.J. Smola, and S. Canu, in Proceedings of the 22nd international conference on Machine learning (2005) pp. 489–496.
[41] P. Goldberg, C. Williams, C. Bishop, Advances in neural information processing systems 10 (1997).
[42] S. Jin, A. Iquebal, S. Bukkapatnam, A. Gaynor, Y. Ding, J. Manuf. Sci. Eng. 142 (2020).
[43] R. Saunders, A. Rawlings, A. Birnbaum, A. Iliopoulos, J. Michopoulos, D. Lagoudas, A. Elwany, Integrating Materials and Manufacturing Innovation 11 (2022) 497.
[44] M.A. Mahmood, A.U. Rehman, B. Karakaş, A. Sever, R.U. Rehman, M.U. Salamci, M. Khraisheh, J. Mech. Behav. Biomed. Mater. 135 (2022) 105428.
[45] X. Gong, Y.C. Yabansu, P.C. Collins, S.R. Kalidindi, Materials 13 (2020) 4641.
[46] Z. Zhu, N. Anwer, Q. Huang, L. Mathieu, CIRP Ann. 67 (2018) 157.
[47] S.H. Lee, Metals 10 (2020) 461.
[48] J. Li, R. Jin, Z.Y. Hang, Materials & Design 139 (2018) 473.
[49] F. Asadi, A. Olleak, J. Yi, Y. Guo, in: in 2021 American Control Conference (ACC), IEEE, 2021, pp. 508–513.
[50] D. Duvenaud, J. Lloyd, R. Grosse, J. Tenenbaum, and G. Zoubin, in Proceedings of the 30th International Conference on Machine Learning, Proceedings of Machine Learning Research, Vol. 28, edited by S. Dasgupta and D. McAllester (PMLR, Atlanta, Georgia, USA, 2013) pp. 1166–1174.
[51] D. Chernyavsky and D. Kononenko, A realization of the heteroscedastic gaussian processes algorithm, https://github.com/Letyachee/hgpr (2023).
[52] A.E. Teschendorff, Nature materials 18 (2019) 422.
[53] X. Li, M. Roberts, S. O'keeffe, T. Sercombe, Materials & Design 112 (2016) 217.
[54] E. Hüllermeier, W. Waegeman, Machine Learning 110 (2021) 457.
[55] A. Der Kiureghian, O. Ditlevsen, Structural safety 31 (2009) 105.
[56] R.-R. Griffiths, A.A. Aldrick, M. Garcia-Ortegon, V.R. Lalchand, A.A. Lee, Machine Learning: Science and Technology 3 (2021).
[57] A. van den Beukel, J. Sietsma, Acta Metall. Mater. 38 (1990) 383.
[58] K. Kosiba, S. Scudino, J. Bednarcik, J. Bian, G. Liu, U. Kühn, S. Pauly, Phys. Rev. B 102 (2020) 134113.
[59] S.V. Madge, A.L. Greer, Oxford Open, Mater. Sci. 1, itab015 (2020).
[60] C. Schick, Anal. Bioanal. Chem. 395 (2009) 1589.